NanoBiotechnology

ISSN 1551-1286/05/01:7–22/$30.00
DOI: 10.1385/Nano:1:1:7

Original Article

Visualizing Nature at Work from the Nano to the Macro Scale

Michel F. Sanner,[1] Martin Stolz,[2] Peter Burkhard,[3] Xiang-Peng Kong,[4] Guangwei Min,[4] Tung-Tien Sun,[5] Sergey Driamov,[6] Ueli Aebi,[2] and Daniel Stoffler[1,2]

[1]Molecular Graphics Laboratory, Department of Molecular Biology, The Scripps Research Institute, La Jolla, CA 92037, USA; [2]M.E. Müller Institute, Biozentrum, University of Basel, CH-4056 Basel, Switzerland; [3]The Institute of Materials Science, University of Connecticut, Storrs, CT 06269-3136, USA; [4]Skirball Institute of Biomolecular Medicine, Department of Biochemistry, and [5]Departments of Dermatology Pharmacology and Urology; New York School of Medicine, New York, NY 10016, USA; [6]Research Department of the University Hospital Basel, Kantonsspital Basel, CH-4031 Basel, Switzerland

Abstract

Visalizing the structure and dynamics of proteins, supramolecular assemblies, and cellular components are often key to our understanding of biological function. Here, we focus on the major approaches in imaging, analyzing, and processing biomedical data ranging from the atomic to the macro scale. Relevant biomedical applications at different length scales are chosen to illustrate and discuss the various aspects of data acquisition using multiple modalities including electron microscopy and scanning force microscopy. Moreover, powerful scientific software is presented for processing, analyzing, and visualizing heterogeneous data. Examples of using this software in the context of visualizing biological nano-machines are presented and discussed.

(Nanobiotechnology DOI: 10.1385/Nano:1:1:7)

Key Words: Electron microscopy; scanning force microscopy; nanoparticles; urinary tract infection; nuclear pore complex; osteoarthritis; atherosclerosis; data visualization; molecular modeling; visual programming.

Correspondence and reprint requests to:
Ueli Aebi
M.E. Müller Institute,
Biozentrum, University of Basel,
CH-4056 Basel, Switzerland
E-mail: Ueli.Aebi@unibas.ch

Daniel Stoffler
Molecular Graphics Laboratory,
Department of Molecular Biology,
The Scripps Research Institute,
La Jolla, CA 92037, USA
E-mail: Daniel.Stoffler@unibas.ch

Humana Press

Introduction

Nanobiotechnology combines nanotechnology with biotechnology to design and produce functionalized biological materials or devices that take advantage of elements or effects that occur at the nanometer scale (for an excellent overview see ref. *1*). These novel materials and devices are expected to impact biomedical areas such as minimally invasive diagnostics and therapeutic interventions.

The enormous potential of nanobiotechnology derives from its interdisciplinary nature, spanning across all fields of science, engineering, technology, and potential applications. However, significant advances in nanobiotechnology and related fields will not be realized without considerable research and development. For example, technologies are needed to visualize, analyze, and manipulate matter at the single-event level, i.e., at the level of single atoms or molecules. Visualizing biological matter at this level of detail will offer important mechanistic insights into biological function by decomposing the ensemble into its elementary components and functional steps.

Over the past decade, various imaging technologies have emerged, enabling researchers to study biological processes at different levels of resolution. Electron microscopy (EM) covers the widest range of dimensions, capable of visualizing whole cells as well as individual biomolecules, their submolecular

structure, and, ultimately, individual atoms *(2,3)*. However, the high vacuum inside the EM instrument causes the biological specimen to dehydrate, leading to preparation artifacts. Embedding the specimen in a thin layer of amorphous ice helps to avoid this dilemma *(4)*. X-ray crystallography and solid-state nuclear magnetic resonance (NMR) spectroscopy provide structural insights with atomic details. X-ray crystallography was the first method for structure determination of single biomolecules. It is still the predominant source for obtaining atomic resolution information of biomacromolecules, ranging from peptides to entire virus particles (reviewed in ref. *5*). NMR is particularly well suited for small molecules, allowing the study of biomolecules in solution *(6)*. Yet, for both methods, there is a theoretical size limit for the sample to be studied, which renders the structure elucidation of larger supramolecular assemblies unlikely using these two methods.

Recently, the scanning force microscope (SFM)—a member of the family of scanning probe microscopes—has opened completely new perspectives for analyzing biological matter in its aqueous environment and at a resolution comparable to that achieved by EM *(7,8)*. The SFM allows visualizing the surface topography, thus providing only limited insight into the internal structure of a given specimen. However, while EM, X-ray crystallography, and NMR spectroscopy only provide snapshots of biomolecules or supramolecular assemblies in distinct functional states, time-lapse SFM enables imaging one and the same specimen in various stages of activity. Hence, the SFM has become a method of choice for directly correlating structural and functional states of biological matter at submolecular resolution *(9–11)*.

Each of these imaging techniques has strengths and weaknesses. A given method either provides only partial insight or is subject to preparative and/or experimental artifacts due to the size and complexity of the specimen under investigation. Therefore, structure determination is best achieved with a hybrid approach where experimental data are gathered by different data acquisition methods and under a variety of preparation conditions.

The task of combining, visualizing, and interpreting the collected data represents yet another major phase in the process of elucidating and making plausible biological function. Powerful software tools such as discussed below aid researchers to integrate heterogeneous data sets recorded by multiple data acquisition modalities into useful and usable models of complex componentry. The emerging models deepen our understanding of structure and function, sharpen our ability to ask the next best questions, and, ultimately, provide us with the capability to develop a realistic chemical and/or physical description of all biological processes at the single-event level.

Designing Peptidic Nanoparticles for Synthetic Vaccine Design, and Local Diagnosis and Intervention

Visualizing viral proteins and assemblies have yielded considerable insight into the workings of molecular machines *(12)*, opening new modalities for diagnostic and therapeutic medical interventions that are minimally invasive and minimize side effects. For example, the combined effort of EM and X-ray crystallography revealed that virus function is largely related to the geometry of their supramolecular assemblies. Accordingly, the capsid of many small viruses is constructed from a regular array of proteins forming an icosahedral shell. In the case of influenza virus and other enveloped viruses, a complex rearrangement process of the surface protein hemagglutinin facilitates the cell penetration.

More recently, it has been demonstrated that it is possible to imitate the viral capsid structure with *de novo* designed artificial proteins or peptides that are able to self-assemble into icosahedral nanoparticles *(13)*. The design principles for these nanoparticles were deduced from visualizing the icosahedral geometry of the capsid architecture of small viruses, combined with a careful analysis of α-helical coiled-coil interactions in the context of protein oligomerization *(14,15)*. As documented in Figs. 1 and 6, icosahedral symmetry involves a geometrical arrangement that is characterized by twofold, threefold, and fivefold rotational axes of symmetry. The same symmetry elements can also be found with multistranded coiled-coils, which represent the most frequently encountered oligomerization motifs of proteins *(16,17)*. Employing molecular modeling and simulation programs, different coiled-coil and other oligomerization domains have been combined into novel protein folds, which might ultimately exhibit the same self-assembling properties as icosahedral virus capsids. An example of such a *de novo* design is shown in Fig. 1: The threefold coiled-coil trimerization domain of fibritin, which had previously been used successfully to initiate proper oligomerization of an otherwise unstable collagen peptide *(18)*, has been linked to the coiled-coil pentamerization domain of COMP *(19)* to correctly reproduce the relative three-dimensional (3D) configuration of the threefold and fivefold symmetry elements of an icosahedral virus capsid. The twofold symmetry element was then generated by interactions between these two domains. Visualizing these protein–protein interactions led to an optimized design.

The rational design of such synthetic peptidic nanoparticles opens a vast number of novel applications in nanobiotechnology and, especially, in nanomedicine. Because these nanoparticles are built from proteins, i.e., the same basic building blocks living organisms are made of, they are not only fully biodegradable but also biocompatible. This, in turn, allows for a tailored design of novel drug targeting and delivery systems. For example, grafting somatostatin onto the surface of the nanoparticle allows for highly specific cell or organ targeting of the nanoparticle. More specifically, in this example the particle will be directed to the somatostatin receptor, which is strongly overexpressed on certain types of cancer cells *(20)*. Loading these nanoparticles with, for example, a radioisotope, the targeted cancer cells will be effectively destroyed without doing any harm to the surrounding healthy tissue.

Another, maybe even more promising, medical application in the context of designing synthetic vaccines is to use the

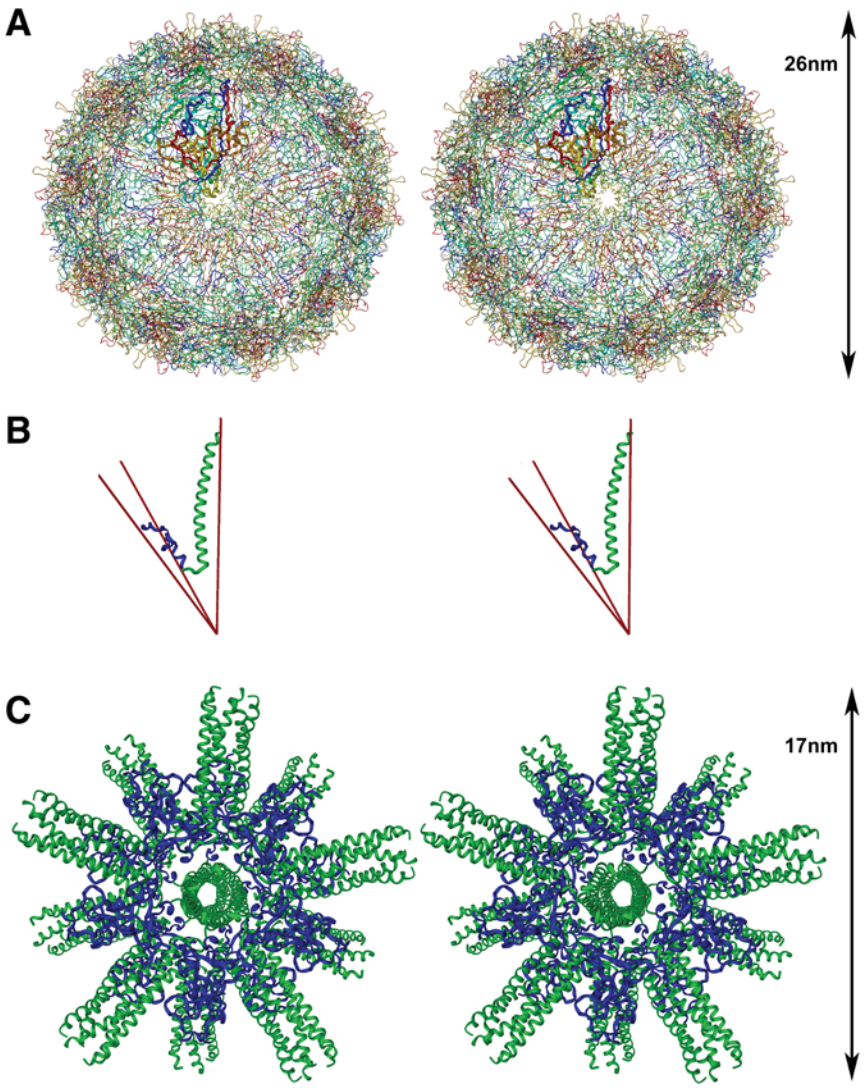

Fig. 1. Design of icosahedral nanoparticles (stereo). (**A**) X-ray crystal structure (1DNV) of the insect parvovirus (*Galleria mellonella densovirus*) with icosahedral symmetry. The protein chains are colored from red (N-terminus) to blue (C-terminus) and one single protein molecule is highlighted. The view is down the fivefold symmetry axis. (**B**) Alignment of the protein oligomerization domains from the fold on domain of fibritin (blue) and the coiled-coil domain of COMP (green) joined into one single peptide chain along the symmetry elements of an icosahedron. The three symmetry axes (twofold, threefold and fivefold) extending from the center of the icosahedron are shown as red lines. (**C**) Applying the symmetry elements of the icosahedron to the peptide chain of section **B** generates an artificial nanoparticle with icosahedral symmetry (the view is down the fivefold symmetry axis as in section **A**).

peptidic icosahedral nanoparticles for repetitive antigen display *(21–23)*. The highly repetitive geometry of the nanoparticle and its resemblance to a small virus capsid will trigger a high-titer/high-affinity and often monospecific immune response. This concept is now increasingly being employed for producing novel vaccines that yield high titers of specific antibodies using virus-like particles as repetitive antigen display systems *(24–27)*. Compared to virus-like particles, such *de novo* designed peptidic icosahedral nanoparticles eliminate the need for virus-based designs, thereby providing increased flexibility in synthetic vaccine design. Epitopes of any pathogen can easily be grafted onto the surface of the nanoparticle, thus allowing for the easy generation of a large variety of different vaccines against pathogens like malaria, HIV, influenza, or many others.

Visualizing the Nanostructure of the Apical Surface of Mammalian Bladder Urothelial by Quick-Freeze/Deep-Etch, Scanning Force Microscopy and Cryoelectron Microscopy

In the following example, with a hybrid approach of EM and SFM, structural information about the urothelial apical

surface was gained at different levels of resolution. The combined analysis and visualization of these heterogeneous data sets allowed for a nanostructural understanding of the apical surface of the bladder urothelium and, in turn, provided novel insights toward a more mechanistic understanding of urinary tract infection.

Accordingly, the apical surface of the mammalian bladder urothelium is covered almost entirely by rigid-looking, concave membrane plaques consisting of 16-nm protein particles that naturally form two-dimensional (2D) crystals *(28)*. These distinct particles, called the asymmetric unit membrane or AUM, are comprised of four integral membrane proteins, the uroplakins (UPs) Ia, Ib, II, and III, that are synthesized as major differentiation products of the urothelium *(29)*. While UP II and III are single-transmembrane-segment proteins, UP Ia and Ib possess four transmembrane segments. UP Ia and Ib are members of the so-called "tetraspanin" family that includes many leukocyte membrane proteins such as CD9, CD81, CD82, and CD151 *(29)*. These tetraspanins may serve as facilitators of forming signaling networks on the cell surface. The urothelial plaques play important roles in urothelial function and diseases, including (i) the permeability barrier function to protect the underlining tissues from the potential harmful components of the urine; (ii) the reversible adjustment of the apical urothelial surface area during the urination cycle; and (iii) the receptor function for the uropathogenic type 1-piliated bacteria, which cause the majority of urinary tract infection (UTI), one of the most common bacterial diseases *(29,30)*.

The distinct nanostructure of the urothelial plaque offers an ideal system for membrane visualization using EM, SFM, and other biophysical tools. Early studies of negatively stained urothelial plaques by EM coupled with image processing revealed that each of the 16-nm uroplakin particles consists of six inner and six outer subdomains that are interconnected to form a "twisted ribbon-like" structure *(31)*. More recent studies of the urothelial plaque using quick-freeze/deep-etch, SFM, and cryo-electron microscopy (cryo-EM) have provided new insights into the structure–function relationships of this remarkable supramolecular nanostructure *(32)*.

Mouse urothelium was examined using the quick-freeze/deep-etch specimen preparation technique, which preserves particularly well the surface topography of membranes and their fractured surfaces (Fig. 2). Cryo-EM observation revealed two features of the urothelial surface that were previously not well understood *(33)*. First, the crystalline array of the uroplakin particles seems to be exposed without an extensive glycocalyx shield (Fig. 2A), suggesting that the apical surface of the urothelial plaque, which contains uroplakin receptors for the type 1-fimbriated *Escherichia coli*, is directly exposed to urine and to invading bacteria. Second, the data show that the regions, which interconnect the crystalline urothelial plaques, known as the "hinges," are very dynamic. Small faults can form within the hexagonal arrays, where individual uroplakin particles can deform and later disappear, thus forming a new particle-free hinge area (Fig. 2B). These results indicate that both uroplakin particles and plaques can undergo dynamic structural changes. Such a dynamic behavior may play a central role in plaque formation and regulation *(33)*.

SFM, which is particularly suitable for studying the surface topography of native biomembranes, was employed to examine the luminal and cytoplasmic surfaces of mouse and bovine urothelial plaques *(34)*. As displayed in Fig. 2C, D, and the upper left of 2G, the luminal surface of the urothelial plaque is characterized by an hexagonal array of 16-nm particles, which exhibit an overall configuration very similar to that revealed by quick-freeze/deep-etch EM [Fig. 2A,B *(33)*] and cryo-EM *(32)*. In addition, the SFM provides an accurate measure of the height of the 16-nm uroplakin particles and the thickness of the lipid bilayer. The information on the height of the particle and how it is placed in the lipid bilayer is important for a better understanding of the molecular architecture of the particle. Early estimates of the height of the 16-nm particle were made by measuring the membrane thickness from thin-section micrographs. However, the accuracy of such measurements was very limited due to various staining and shrinkage artifacts. Furthermore, SFM revealed for the first time a cytoplasmic protrusion of the uroplakin particle (Fig. 2E,F). Previously, the issue of whether the urothelial particle protrudes the cytoplasmic surface of the urothelial plaque was controversial. Early EM studies indicated that the cytoplasmic face of the plaque was very smooth; in fact, it was even suggested based on some EM fracture data that the urothelial particle "floats" on the exoplasmic surface of the plaque without actually penetrating the lipid bilayer. Even cryo-EM, the best method to visualize the entire particle including the transmembrane domain, cannot determine the precise boundaries of the lipid bilayer and whether the 16-nm particle harbors a significant cytoplasmic protrusion. Employing different adsorption conditions, both the luminal and cytoplasmic face of the urothelial plaques were visualized by SFM *(34)*. These data clearly document that the 16-nm uroplakin particle exhibits a 0.5-nm circular cytoplasmic protrusion (Fig. 2E,F, and the lower right of 2G). This observation is consistent with the current notion, i.e., based on their primary sequences, that all uroplakin subunits are integral membrane proteins and harbor at least one transmembrane segment.

Cryo-EM, which is ideally suited to visualize the native uroplakin particle including its transmembrane domains, was employed to obtain a 3D structure of the entire 16-nm uroplakin particle *(32)*. To achieve this, low-dose tilt-series of frozen-hydrated mouse urothelial plaques were recorded, from which a 3D reconstruction of the urothelial particle was computed, with 10-Å resolution in the membrane plane and 16.5-Å in the vertical direction (Fig. 2H,I). These results confirmed that the 16-nm urothelial plaque particle consists of six inner and six outer cylindrical subdomains both of which traverse the entire lipid bilayer, and allowed the construction of a urothelial plaque model, which reveals the following salient features: (i) Over

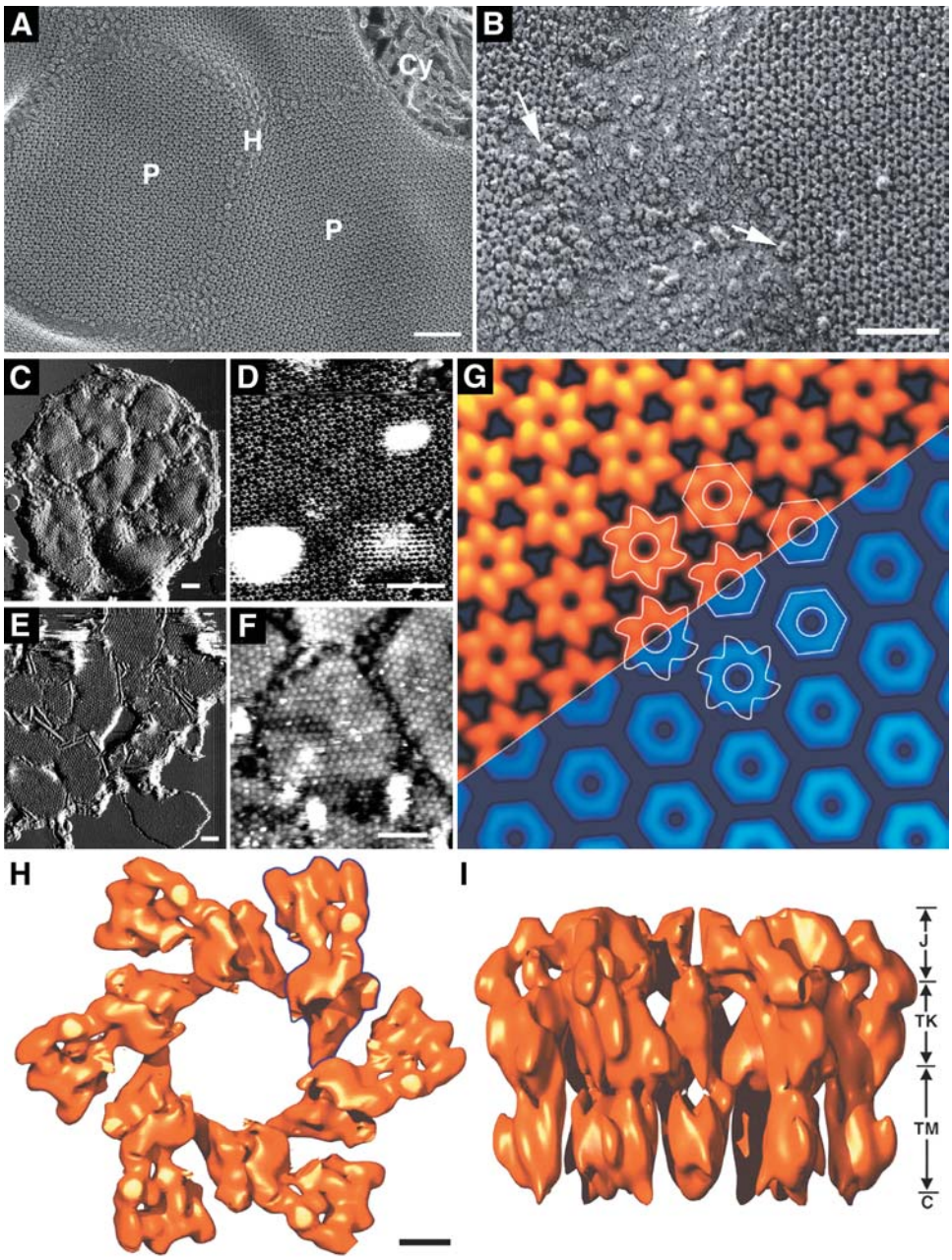

Fig. 2. Visualization of the 16-nm uroplakin particles on the mammalian urothelial surface. (**A,B**) Quick-freeze/deep-etch (QFDE) and rotary shadowed images of the mouse urothelial surface. (**A**) An overview showing several urothelial plaques (P) interrupted by hinge regions (H). The plasma membrane at the upper right corner is fractured revealing an exposed cytoskeleton (Cy). (**B**) A detailed QFDE view of a hinge region showing uroplakin particles undergoing desegregation and deformation (arrows). (**C–G**) Surface topography of the 16-nm particle by SFM. (**C**) Low magnification view of the luminal face of several interconnected mouse urothelial plaques. (**D**) High-magnification view of the luminal surface of a mouse urothelial plaque. (**E**) Low-magnification view of the cytoplasmic face of several bovine urothelial plaques. (**F**) High-magnification view of the cytoplasmic face of several bovine urothelial plaques. (**G**) The averaged images of the luminal (upper left half in red) and cytoplamic (lower right half in blue) surfaces of mouse and bovine, respectively, urothelial plaques. Scale bars, 100 nm (**C–F**). (**H,I**) A 10 Å resolution 3D structure of the 16-nm uroplakin particle by cryo-electron microscopy (cryo-EM). (**H**) The top view of the 3D density map of a mouse 16-nm uroplakin particle that is contoured at 1.5σ level. The boundary of a "subunit" consisting of an inner and an outer subdomain is outlined (in blue). (**I**) The side view of the 16-nm particle showing, from top to bottom, the joint (J), trunk region (TK), transmembrane domain (TM), and cytoplasmic domain (C). **H** and **I** are of the same scale; the bar in **H** denotes 2 nm.

60% of the urothelial plaque surface area appear to be occupied by lipids that, via their interaction with the crystalline uroplakin network, may assume a highly ordered conformation thus contributing to the permeability barrier function of the urothelium. (ii) The cryo-EM structural data, combined with previous chemical crosslinking and uroplakin localization data, suggest that the uroplakin pairs UP Ia/II and UP Ib/III occupy the inner and outer subdomains, respectively, of the 16-nm particle (see Fig. 2H). (iii) Each outer subdomain of the 16-nm particle is connected at its distal end to a neighboring inner subdomain via a "joint" which may allow the two subdomains to twist relative to each other, thereby providing a possible mechanism for transmitting signals across the urothelial apical membrane upon binding of a bacteria that may lead, in turn, to the invasion of the attached bacteria *(32)*.

Cryo-electron Microscopy and Time-Lapse Scanning Force Microscopy of the Nuclear Pore Complex Provide Novel Mechanistic Insights into Nucleocytoplasmic Transport

Nuclear pore complexes (NPCs; Fig. 3) are large macromolecular assemblies with a mass in excess of 100 MDa *(35)* embedded in the double-membraned nuclear envelope (NE). They represent the major gateways mediating transport of ions, small molecules, proteins, RNAs, and ribonucleoprotein particles in and out of the nucleus in interphase cells (reviewed in ref. *36*). However, despite much progress in recent years, the exact molecular mechanisms underlying nucleocytoplasmic transport and, in particular, cargo translocation through the NPC are still understood rather poorly.

NPCs are rather dynamic supramolecular assemblies, where significant structural changes can be induced by cellular signals such as calcium or nucleotides *(36,37)*. Hence, identification, characterization, and visualization of distinct functional states of the NPC will be a prerequisite to pursue a structure-based functional analysis of nucleocytoplasmic transport at the molecular level, in particular, to follow cargo translocation through the NPC.

3D reconstructions from electron micrographs of amphibian oocyte NEs have provided considerable insights into the 3D architecture of the NPC and thereby enhanced our understanding of nucleocytoplasmic transport *(36)*. Moreover, during the past several yrs significant progress has been made toward identifying and characterizing distinct NPC subcomplexes (reviewed in refs. *38* and *40*) *(39)*. Cryo-electron tomography (cryo-ET) of fully native NPCs (i.e., without detergent treatment, chemical fixation, or dehydration/rehydration during preparation steps) from *Xenopus* oocyte NEs embedded in thick ice (Fig. 3A) has revealed a number of distinct structural features (Fig. 3B) *(41)*. More specifically, the cytoplasmic face of the NPC harbors distinct anchoring sites for the cytoplasmic filaments, and the nuclear face is topped with a massive distal ring positioned above the central pore with indications of the anchoring sites for the nuclear basket filaments and putative intranuclear filaments. Also, the rather "spongy" central framework of the NPC is perforated by an elaborate channel and void system, whereas the membrane–pore interface exhibits distinct "handles" protruding into the lumen of the NE. The most variable structural moiety of the NPC is a rather tenuous central plug (discussed below), partially obstructing the central pore. Its mobile character was documented by SFM *(10,41)*. More recently, these structural features have been confirmed and elaborated further by investigating transport-active, intact nuclei from *Dictyostelium discoideum* by means of cryo-ET *(42)*. These structural insights gained into NPC architecture support the notion that the NPC acts as a constrained diffusion pore for molecules and particles without retention signal and as an affinity gate for signal-bearing cargoes *(36,40)*.

Furthermore, time-lapse SFM enabled for the first time the direct observation of distinct structural changes at the level of individual NPCs under various physiological conditions *(10)*. For this to be achieved, fully native *Xenopus* oocyte NEs were prepared on a solid support with either their nuclear or cytoplasmic face immobilized and imaged by SFM in physiological buffer (Fig. 3C,D). In response to adding or removing calcium, the repeated opening and closing of the nuclear basket of individual native NPCs could be observed without, however, affecting the overall height and shape of the basket (Fig. 3E,F). The observed 20–30 nm diameter openings may be interpreted in terms of the nuclear basket's distal ring acting as an "iris-like" diaphragm, which is closed in the absence of calcium and opens upon addition of calcium (Fig. 3E,F, right panels).

Based on these observations, it was hypothesized that the distal ring of the nuclear basket might be involved in mediating nucleocytoplasmic transport. Recent findings documenting the mobile character of the vertebrate nucleoporin Nup153 support this possibility *(36,43)*. Accordingly, Nup153 appears to be anchored to the distal ring through its central zinc-finger domain and to the nuclear ring moiety through its amino-terminal domain. In contrast, the carboxy-terminal domain of Nup153, composed of approx 40 phenylalanine–glycine (FG) repeats, appears highly mobile, as it could be mapped to the nuclear ring moiety, the distal ring, and even the cytoplasmic periphery. Furthermore, it has been documented that Nup153 plays an important role in protein import as a terminal docking site *(44)*, as well as in mRNA export *(45)*. Hence, it is conceivable that Nup153 with its Zn-finger domain acts as a structural scaffold of the eightfold symmetric distal ring, which might act as a ligand-sensitive docking or even a gating site for cargo transported in and out of the nucleus. In addition, the highly mobile FG-repeats might increase the efficiency of cargo translocation through the NPC *(36)*. In contrast to the calcium-induced effects observed on the nuclear face of the NE, the cytoplasmic face appears rather unaffected by the same treatment *(10)*. However, calcium also significantly affects the conformation of the central framework of the NPC [Fig. 3G,H *(41)*].

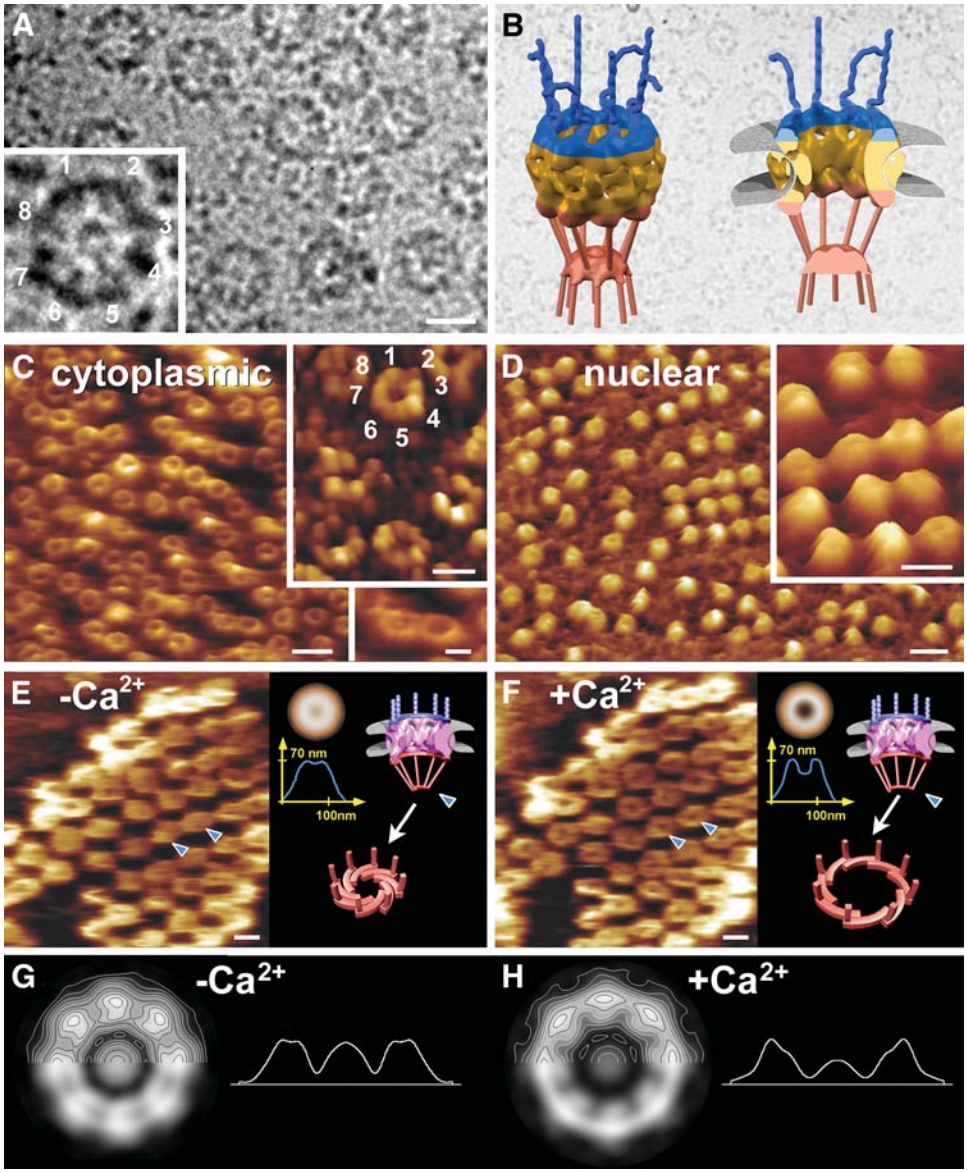

Fig. 3. Visualization of native nuclear pore complexes (NPCs) by cryo-EM and SFM. (**A**) Appearance of thick ice (>200 nm) embedded, chemically unfixed, and unstained native *Xenopus* nuclear envelope (NE) spread over a perforated carbon support film imaged by zero-loss energy-filtering transmission electron microscopy (EFTEM). The overall eightfold rotational symmetry, and the nuclear basket and its distal ring are readily visible (inset). (**B**) The visual programming environment "Vision" (see Fig. 6) was used to build a new structural consensus model of the NPC. The cytoplasmic filaments (blue) and the struts of the nuclear basket (orange), absent in the cryo-EM tomographic 3D reconstruction due to their inherent flexibility, were modeled into the 3D reconstruction based on thin-section images (where the filaments are visible) and height measurements of the nuclear basket (see **D–F**) by scanning force microscopy (SFM). Corresponding SFM images of native NPCs kept functional in near-physiological buffer reveal a distinct morphology for the cytoplasmic (**C**) and the nuclear face (**D**) of spread *Xenopus* NEs. The insets in **C** depict a high-magnification view of the rotational symmetry of individual NPCs (top) as seen in **A** and NPCs with clearly visible "plugs" (bottom). The inset in **D** depicts a high-magnification view of the nuclear baskets. **C** and **D** were tilted 80° using the scanner software to improve the 3D appearance. **E** and **F** reveal reversible calcium-mediated structural changes of the nuclear baskets (i.e., the distal rings) by time-lapse SFM of the same individual NPCs. In the absence of calcium, the distal rings are "closed" (**E**). Adding 100 μM Ca^{2+} to the buffer medium opens the distal rings (**F**). This process is reversible (for example, by adding 1 mM EGTA which selectively chelates calcium). Calcium only affects the opening of the distal ring of the nuclear basket, not its overall height, as shown in the averaged radial height profiles in **E** and **F**. The 3D models in **E** and **F** depict the tentative interpretation of the opening and closing of the distal ring upon changing the calcium concentration. In this model, the distal ring might act as an iris-like diaphragm. For better comparison, the same individual NPCs were marked with blue arrowheads. **G** and **H** Single-particle averages, both displayed as gray-level/contours representations and radial mass density profiles of 100 NPCs each in the absence and presence of calcium revealed significant structural rearrangements within the entire NPC. Scale bars, 100 nm (**A–F**).

Despite much recent progress made toward a better understanding of the 3D architecture of the NPC, the identity, molecular composition, and functional significance of some of its components have remained controversial, for example, the central plug. In 2D projection images, the central pore of the NPC often appears obstructed by a particle that varies greatly in size and shape (Fig. 3A). This particle is commonly referred to as the central plug or transporter. On the basis of such projection images, it was assumed that the central plug represents a *bona fide* stationary component of the NPC, probably involved in mediating nucleocytoplasmic transport. However, the recent 3D reconstructions of native NPCs *(41,42)* and time-lapse SFM experiments *(10,41)* have provided strong evidence that in projection images such as Fig. 3A, the central plug most probably results from superposition of the distal ring and cargo caught in transit while translocating through the central pore of the NPC. This latter view is also strongly supported by the recent findings that the central plug/transporter is variable in shape and volume and can occupy different positions along the nucleocytoplasmic axis of the NPC *(42)*.

Revealing distinct functional states of the NPC by hybrid imaging modalities has led to a new consensus model (Fig. 3B), providing valuable insight toward a more structural understanding of the conformational dynamics exerted by supramolecular machines. Ultimately, this consensus model may also serve as a framework for mapping the individual nucleoporins or distinct NPC subcomplexes—once their atomic structures have been determined—within the 3D architecture of the NPC. Such pseudo-atomic models in distinct functional states will be key toward a more mechanistic understanding of nucleocytoplasmic transport, particularly of cargo translocation through the NPC's central pore. Ultimately, the NPC may become a role model for directly correlating structural data with functional states and dynamic features of living matter at the level of individual supramolecular machines.

Scanning Probe Devices Will Aid Surgeons to Assess the Biomechanical Properties of Normal, Diseased, and Engineered Tissue

As discussed above, a detailed understanding of biological systems at the molecular level and beyond will serve as a framework for developing new therapeutic concepts. For example, during the past century the average life expectancy has increased by nearly 20 yr. While this definitely represents an unprecedented achievement, this gain is still at the expense of numerous diseases that are becoming more prominent in the elderly. Hence, an accurate diagnosis is important at an early stage of disease progression, hopefully at a stage where the disease might still be halted or even reversed. Efforts toward miniaturizing diagnostic devices, and the development of new medical technology and inspection protocols toward early diagnosis, are in progress and provide us with a variety of new visualization techniques. Moreover, minimally invasive surgery, for example, with a laser beam, allows more precise and less damaging interventions. However, despite all these advances, detailed structural and functional information at the level of living cells or smaller cannot be obtained with instruments currently used in the clinic *(46,47)*.

Novel devices based on the SFM, one of the principal tools of nanoscience [see above *(7,8)*], can be used for investigating a variety of interesting targets of the body. One major advantage of the SFM is the fact that in addition to visualizing, it can also measure and manipulate biological tissue *in situ* and in its physiological environment. Moreover, the SFM allows tissue to be assessed from the cellular to molecular level, i.e., at the scale where biochemical processes occur and, in fact, most diseases start. Accordingly, a large number of diseases are directly based on molecular events occurring at the µm to nm scale, for example, inborn errors of cellular metabolism, virus "docking" and cell invasion, unwanted reactions in transplant rejections, and autoimmune diseases. The following two examples aim toward a better understanding of two frequent and often devastating diseases, osteoarthritis and atherosclerosis.

Osteoarthritis develops over many yrs and typically starts with inoffensive, non-specific aches that then slowly but definitively mature into the full-blown disease. The development of osteoarthritis may be triggered by single events such as a sports injury or a trauma from a traffic accident, as well as by long-term risk factors such as obesity, physical inactivity, stress, and smoking. Even a person with no previous sports injury or trauma from an accident may eventually be affected by osteoarthritis.

The second disease discussed below, atherosclerosis, represents the major cause of death and disability in the First World nations and occurs mostly as a myocardial infarction or stroke. A myocardial infarction is not at all a random event, but has a clear pathophysiologic target: inflammatory processes residing in atherosclerotic plaques lead to rupture of the so-called "cap" of the plaque that finally leads to a blood clot at this location, followed by vessel obstruction, myocardial necrosis, and possibly death. While inflammatory processes strongly influence the development of the vulnerable plaque, the pathogenesis of these cardiovascular events is difficult to diagnose with current tools. Methods to detect vulnerable plaques before they rupture might pave the way toward treatment modalities before a myocardial infarction develops, potentially preventing cardiovascular events in the future. Hence, for exploring osteoarthritis or atherosclerosis, it is important to visualize the morphology and assess the biomechanical properties of the affected tissue at an early stage and to monitor their changes during pathogenesis.

As a first example, normal articular cartilage was imaged with an SFM. The images depict a random orientation of the collagen fibers as illustrated in Fig. 4A, which exhibit a distinct 67-nm axial repeat. For comparison, osteoarthritic cartilage displays a preferred orientation and bundling of the collagen fibers, as marked by the arrows in Fig. 4B. Because of the mechanical stress, it is conceivable that upon degradation of the proteoglycan gel, which is filling the space between the collagen fibers, the collagen fibers are no longer kept apart and coalesce on top of each other,

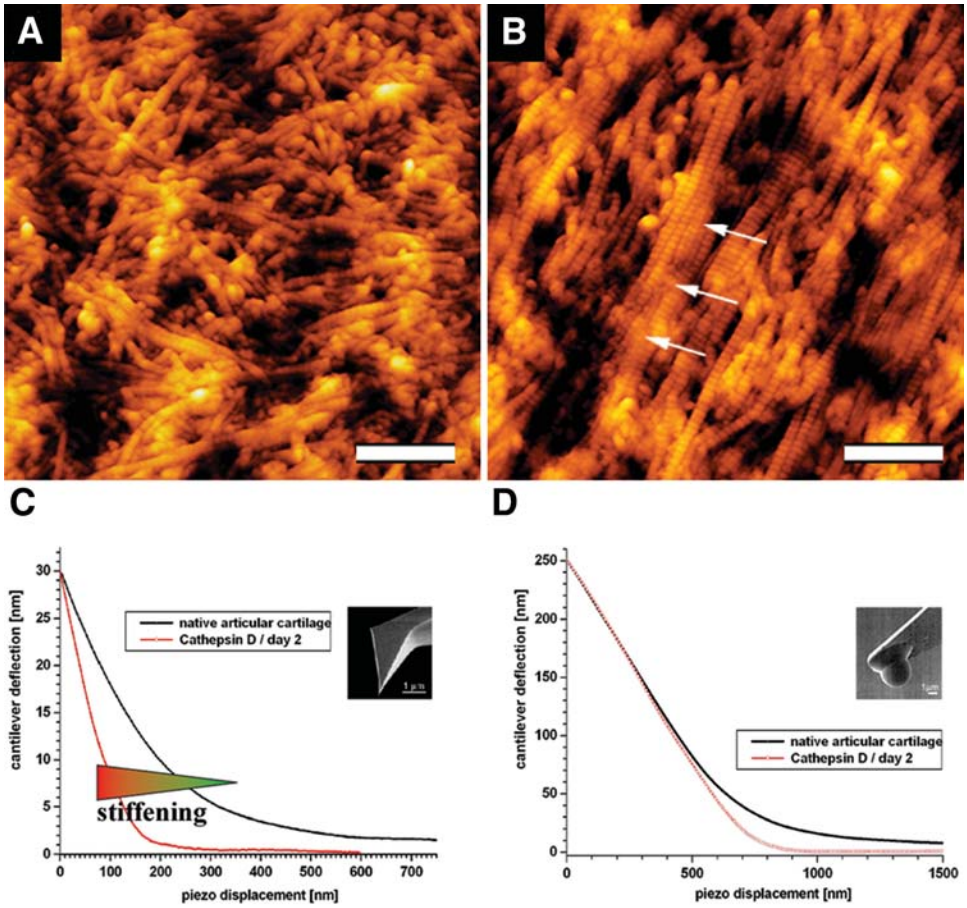

Fig. 4. Surface topography of **A** normal articular cartilage and **B** ostheoarthritic articular cartilage, imaged in air, and (**C, D**) the corresponding elasticity measurement at the nanometer scale. **A** The 67-nm repeat of individual collagen fibers is clearly resolved by SFM. **B** In contrast to the normal cartilage that exhibits a random orientation of the collagen network, in the diseased cartilage the collagen fibers exhibit a preferred orientation and a more dense packing of the collagen fibers. The orientation of the fibers might follow the directed movement within the joint more easily once the glycosaminoglycans become degraded in the course of disease progression. Elasticity measurements were taken of the same samples by employing two different indenter sizes, i.e., (**C**) nanometer-sized sharp pyramidal shaped tips (tip-radius = 20 nm), and (**D**) micrometer-sized spherical tips (tip-radius = 2.5 μm). Each set of the two curves was obtained from normal articular cartilage and from cathepsin D–digested articular cartilage. For digestion the articular cartilage was treated with cathepsin D at 37°C for 2 d. Comparison of the two slopes when recorded on the micrometer scale indicates no difference between native and cathepsin D– treated articular cartilage. At the nanometer scale, however, the cathepsin D–treated articular cartilage exhibits a stiffening compared to the healthy articular cartilage. The two icons in **C** and **D** depict at what spatial level the indenters assay the cartilage architecture, i.e., a micrometer scale indenter (**D**) may simply distinguish between the chondrocytes and the extracellular matrix (ECM), whereas a nanometer scale indenter (**C**) may reveal the distinct fine-structure of the ECM. Such an indenter may probe, for example, the glycosaminoglycan-filled interstitial space between the collagen fibers that is often altered during disease progression. Scale bars, 1 μm (**A** and **B**).

thereby slowly aligning themselves in a direction of the predominant joint movement.

The degradation of the proteoglycan moiety during the progression of osteoarthritis can also be mimicked by ex vivo enzymatic treatment of fresh cartilage with cathepsin D, which selectively digests the proteoglycans while leaving the collagen fibers intact. The elasticity of healthy cartilage and cathepsin D–digested cartilage was assessed with indentation type (IT) SFM, a new method based on the high dimensional sensitivity of the SFM. As documented in Fig. 4C, when probed by IT SFM at the nm-scale, the digested (i.e., osteoarthritic) cartilage appears mechanically significantly stiffer than the healthy cartilage *(48)*. In contrast, IT SFM performed at the μm- rather than nm-scale failed to detect a stiffening of articular cartilage upon degradation of its proteoglycan gel (Fig. 4D). Similarly, current clinical indentation testing devices, which measure cartilage elasticity at the millimeter or centimeter scale, cannot resolve the local, hierarchically organized fine structure of a given tissue sample.

Taken together, this observation opens the exciting possibility that IT SFM, when performed at the nanometer scale, can detect small alterations in stiffness as they are occurring

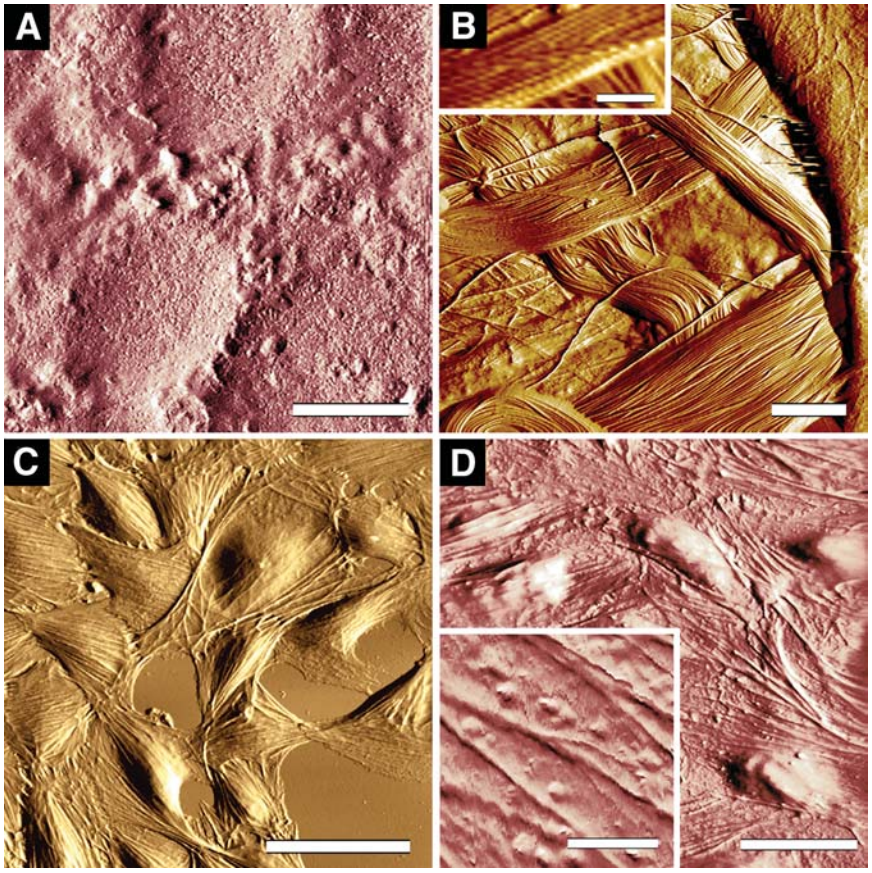

Fig. 5. SFM imaging of native coronary artery tissue. (**A**) SFM imaging reveals the intact endothelial cell layer lining the lumen of a porcine artery in physiological buffer. Individual cells can clearly be delineated, but also their segregating cells junctions. (**B**) The surface endothelial layer of a wild-type mouse coronary artery was mechanically removed by surgical tools for inspection in physiological buffer. The SFM image reveals the subsurface layer that is supporting the endothelium. The inset documents the 67-nm axial repeat of the collagen fibrils. (**C**) SFM imaging of rat-2 cells as imaged under culture conditions. Different cells and their cytoskeletal actin network are visible. (**D**) Cultured HUVEC cells grown as a monolayer on a glass surface and imaged under culture conditions. In contrast to their native environment (i.e., embedded in the extracellular matrix of the coronary arteries), these cultured cells express a distinct network of actin stress fibers. The inset depicts a higher resolution image of HUVEC cells, which exhibit granular structures. Scale bars: 25 μm; inset 2 μm.

at an early stage of osteoarthritis, possibly at a stage when the disease may still be halted. Such early diagnosis, in turn, has the potential to lead to completely new strategies for prevention and/or treatment of osteoarthritis *(48,49)*.

Similarly, exploring the pathogenesis of atherosclerosis by SFM may involve the following experimental approach: (1) Human coronary arteries should be prepared for SFM inspection in a close-to-native state immediately following autopsy. (2) Animal models such as, for example, Apo-E–deficient mice that develop atherosclerotic lesions within a few months in response to particular dietary regimens should be employed to follow so-called "vulnerable plaque" formation *(50,51)*. And (3) cultured endothelial cells serving as an in vitro model should be inspected by SFM to characterize their morphological and biomechanical alterations occurring in response to chemical effectors or physical stimuli *(50,51)*, and to relate these to the human autopsy and Apo-E mice data.

To start, a preparation protocol for SFM was developed that allows studying fresh coronary arteries in a close-to-native buffer environment. Figure 5A displays an example of a freshly prepared endothelial cell layer lining the lumen of a porcine artery in physiological buffer. Individual cells can clearly be delineated, together with their segregating cell junctions. To assess the underlying extracellular matrix, the endothelium of wild-type mouse aorta was removed. The extracellular matrix exhibits an extensive collagen fiber meshwork (Fig. 5B), depicting the distinct 67-nm axial repeat of the collagen fibers (Fig. 5B, inset; see also Fig. 4B). Figure 5C is an example of living rat fibroblasts imaged under culture conditions, which also document the great potential of the SFM for probing biomechanical properties. Figure 5D depicts cultured human umbilical vein endothelial cells (HUVEC) as an additional in vitro model system, imaged under similar conditions as the cultured rat fibroblasts depicted in Fig. 5C. In contrast to their *in situ* environment, i.e., being anchored to the extracellular matrix of a blood vessel, cultured HUVECs that are grown on a glass support exhibit a distinctive network of actin stress fibers very much like the rat fibroblasts (Fig. 5C). Unlike in their native

tissue environment, cultured HUVECs grow much larger (approx 40 μm in diameter), and they reveal "fried–egg"–like elevated cellular nuclei. Examination of these cultured HUVECs at higher magnification yielded distinct granules adhering to the plasma membrane (Fig. 5D, inset) similar to those depicted on the coronary artery endothelial tissue surface (Fig. 5A).

Obviously, the next step is to move these ex vivo and in vitro measurements to *in situ* measurements directly in the patient. To achieve this ambitious goal, the SFM has to be brought to the defect site by an arthroscope, i.e., in the case of osteoarthritis, or a catheter, i.e., in the case of coronary artery atherosclerosis *(49,52,53)*. The ultimate goal here is to study the changes in the pathogenesis of the extracellular matrix in cartilage, and the development and progression of vulnerable plaques, toward a cure and possibly even prevention of these burdens of aging. In the context of new applications of nanotechnology, the arthroscopic SFM might be just the beginning of a new generation of nano-tools for minimally invasive endoscopic interventions. In that perspective, we are still living in the "stone age" of scanning probe–based clinical tools. However, we believe that scanning probe devices will eventually help surgeons to more effectively detect diseases and repair the human body by minimally invasive procedures and therapeutic interventions that minimize side effects.

Interoperable Visualization Tools

As advances in experimental techniques increase our ability to observe biological processes at work, it becomes increasingly important to develop the means to extract, analyze, manage, and communicate the information implicitly and explicitly contained in these data. Today, the visual interpretation of results often determines whether an experiment is continued, terminated, or modified and restarted. However, most scientific visualization, simulation, and analysis tools are being developed for a specific scale, thus hindering the integration of heterogeneous data, which can range all the way from the quantum chemistry level through nano- to macrophysiology. The emerging grid technology (see below) poses additional challenges toward developing the next generation of scientific software tools. The grid infrastructure enables software applications to integrate instruments, displays, and computational and information resources managed by diverse organizations in widespread locations. Such distributed computational resources and data repositories create the need for secure and efficient communication between processes running in distributed hardware environments.

Thus, the next generation of biomedical software applications will have to achieve a high level of flexibility and portability in order to take advantage of the rapidly evolving software and hardware infrastructures, and the ever-growing databases. The hallmark of this software will be the interoperability of computational methods developed across a variety of scientific domains. This requirement will be the key for leveraging scientific expertise, integrate research across scales, and expedite software development through code reuse.

The Molecular Graphics Laboratory (MGL) at The Scripps Research Institute (TSRI) has spearheaded the development of a novel "component-based" software development strategy *(54,55)* centered on the Python programming language *(56)*. The essence of this approach is to use a high-level, general-purpose, interpretive programming language as a computational environment. Rather than writing a standalone program to answer specific scientific questions, the Python interpreter, acting as a framework, is dynamically extended with new software components, which contain specific functionality. These components can be loaded at runtime, effectively augmenting the Python environment with new computational capabilities. Furthermore, Python serves as powerful, yet flexible "glue" for rapidly assembling these software components into custom applications (see below). Python software components can contain code written in compiled languages such as C, C++, or FORTRAN. However, software components written solely using the Python programming language present the benefit of being platform independent, i.e., the same source code runs on any computer running a Python interpreter. This approach strongly promotes code reuse and every computational method that is added to the Python environment automatically becomes interoperable with any application running a Python interpreter. This has to be contrasted with the more traditional "application-centered" approach, where the environment is a program that can be extended by embedding or interfacing new computational methods. In the latter approach, adding a new method usually only benefits that particular program.

The benefits of the component-based approach have already been demonstrated by the creation and wide distribution of a number of scientific visualization tools *(57–59)*. Other scientists developing similar tools have recognized the validity and advantages of this approach and are now progressively adopting this software development strategy *(60)*. It is noteworthy that this software development strategy is application-domain independent, and several of these software components have already found applications beyond the biomedical field.

The rapidly evolving requirements in terms of software integration and combination of computational methods make it impossible for programmers to foresee all possible ways in which users might want to combine software components and tools to advance their research. The concept of "visual programming" provides an elegant solution to this challenge. Here, programming language syntax and data structures are abstracted as graphical icons. A graphical user interface such as depicted in Fig. 6 allows the user to combine these icons interactively to form a computational network. The node icons, which contain the computational methods, are organized into libraries (Fig. 6A) from which they may be drag-and-dropped to a canvas (Fig. 6B). Their input- and output-ports may then be connected to form networks that can be executed like a program (Fig. 6B).

Visual programming has been explored for over two decades in tools such as AVS from AVS Inc. *(61)*, Iris Explorer *(62)*,

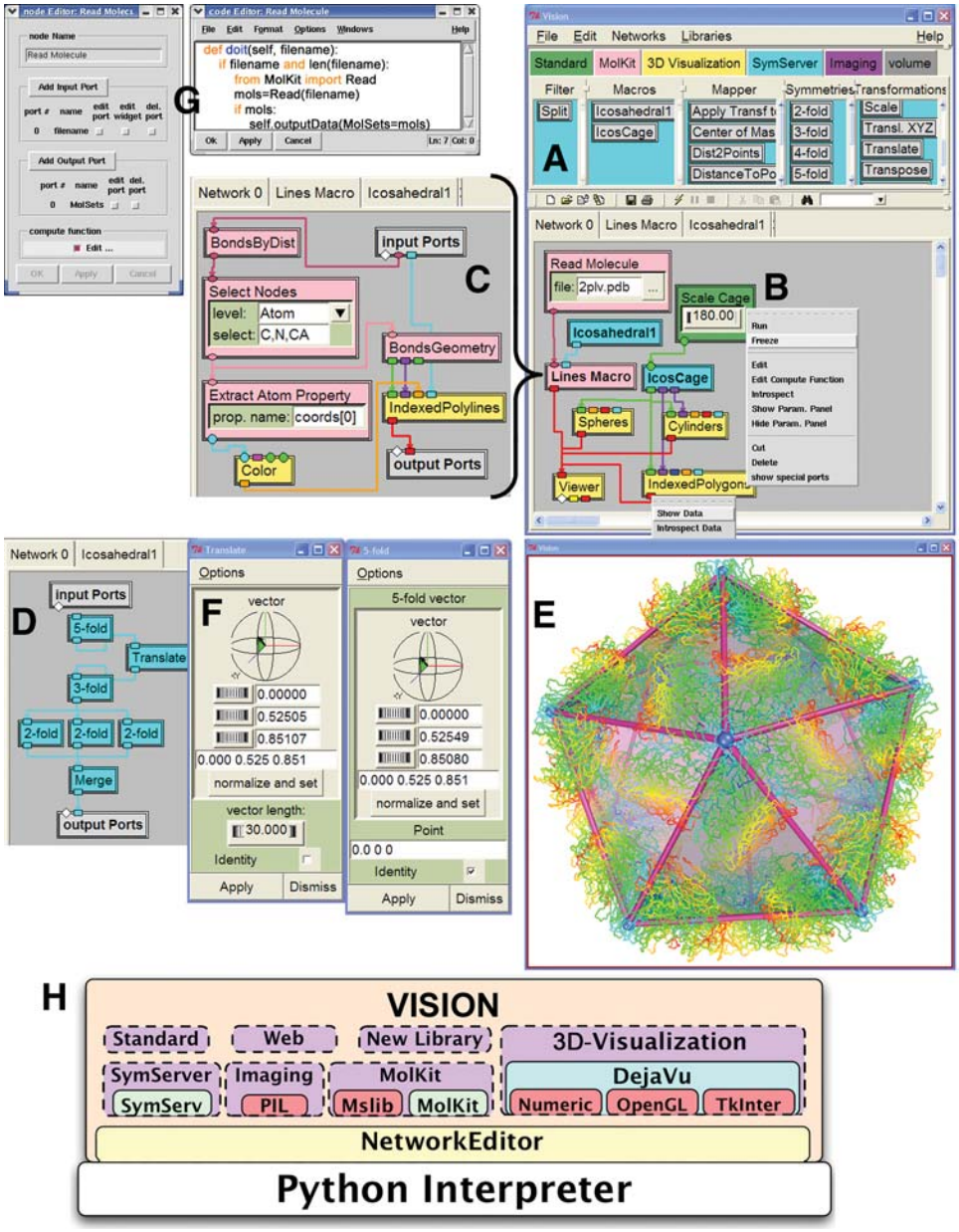

Fig. 6. Vision: a component-based visual programming environment. (**A**) Computational nodes are organized in libraries (i.e., "*Standard,*" "*MolKit,*" etc.). Nodes in a library are grouped by category (i.e., "*Filter,*" "*Macros,*" etc.). Here, the "SymServer" library is shown, exposing nodes for creating point symmetry transformation matrices. (**B**) Nodes can be dragged-and-dropped from the libraries onto a canvas and connected to create computational networks. This particular network reads the poliovirus capsid protein "2plv.pdb," displays its line representation, and duplicates this geometry 60 times with an icosahedral arrangement to depict the complete viral capsid. Note that the nodes in the networks are colored according to their library of origin. (**C**) The lines representing covalent bonds are created by a macro node, i.e., a node in the parent network which contains a subnetwork. (**D**) The macro-network contained within the "*Icosahedral1*" macro-node. This macro computes a list of 60 (4x4)-transformation matrices used to duplicate the line representation of the molecule depicted in (**E**). To obtain the "exploded" view of the viral capsid shown in the interactive 3D viewer (**E**), a "*Translate*" node was inserted below the "*5-fold*" node in (**D**). After setting the translation vector in the "*Translation*" node' parameter panel (**F**) to match the fivefold axis, the thumbwheel widget labeled "*vector length*" allows translating each pentamer along its fivefold axis. (**G**) Nodes in a Vision network can be inspected and modified at runtime. Here, the node editor was started on the "*ReadMolecule*" node. The computational function called "*doit*" runs every time the node is scheduled for execution. This function inputs a file name and uses a function called "*Read*" from the "*MolKit*" software component to open the file, parse its content, and build data structures representing the molecules in the file. The "*MoleculeSet*" object returned by the "*Read*" function is then output on the node's output port.

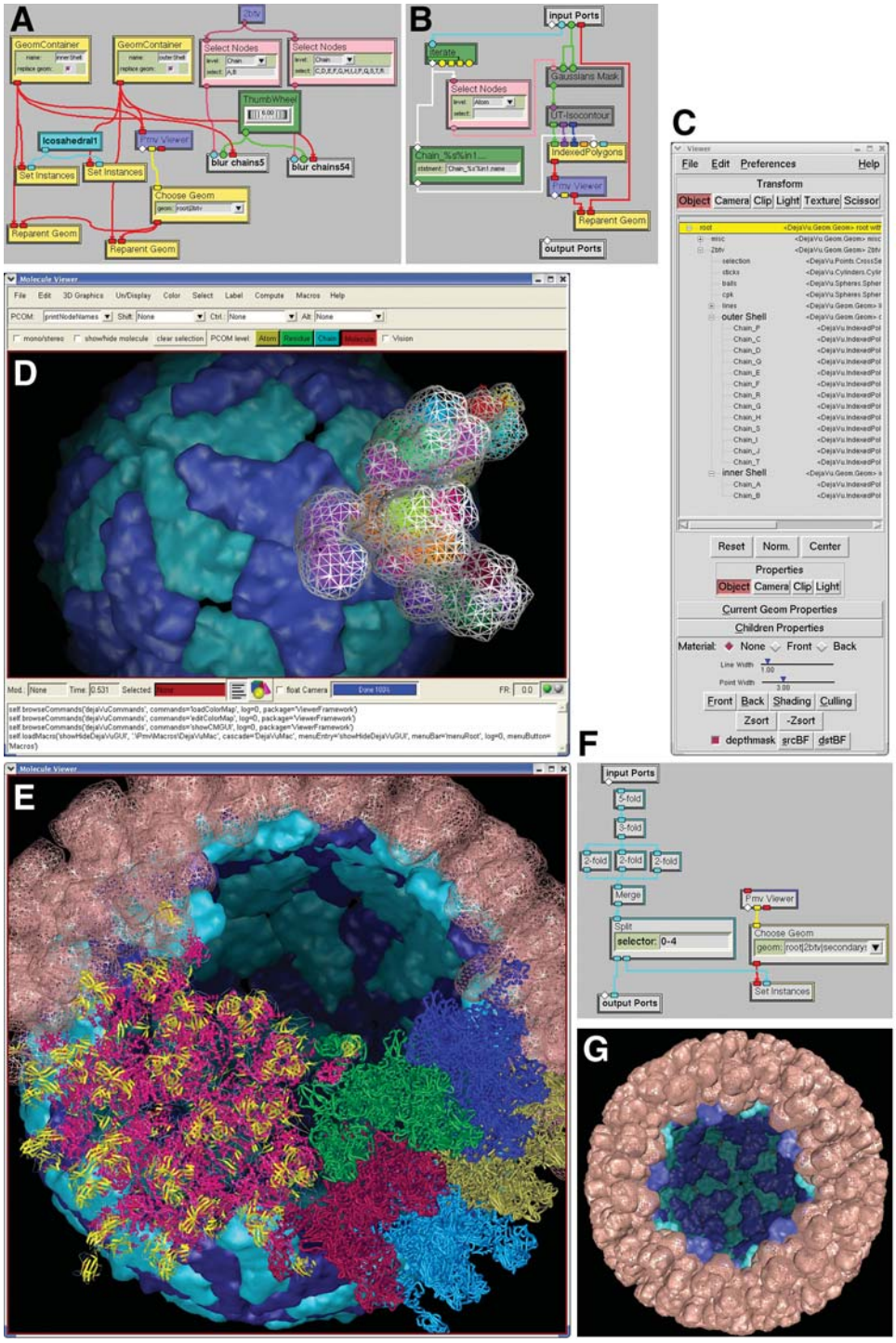

Fig. 7. Prototyping advanced visualizations of the bluetongue virus. The Vision component (**A,B,F**) was started from the Python Molecule Viewer (PMV; see **D**) enabling it to operate on PMV commands and objects. (**A**) A Vision network for creating a separate low-resolution surface for each of the protein subunits in the viral capsid. Two "*GeomContainer*" nodes are used to create the "*inner Shell*" and "*outer Shell*" objects in the geometry hierarchy (**C**) for holding the low-resolution surfaces generated for the individual proteins. The two "*Select Nodes*" extract the proteins of the inner shell and the proteins of the outer shell. These lists of protein-chains are each fed into "*blur chains*" macro nodes. (**B**) The corresponding macro network contained within these nodes iterates over a list of chains and for each chain creates a pseudo density map and computes an isosurface that is added to PMV's 3D viewer and made a child of the appropriate container object. (**C**) The graphical user interface of the "*Pmv Viewer*" node. The hierarchical nesting of geometrical objects allows a user to instantly show or hide a particular viral capsid shell by selecting a container object and switching its visibility flag on or off.

(*Caption continues on p. 20*)

and OpenDX *(63)*. The freely available "Vision" software component [formerly named "ViPEr" *(58)*] developed at TSRI supports the visual programming paradigm (Fig. 6). Although it bears many similarities with tools such as AVS and can be used as a standalone visual programming environment, it is fundamentally different because it was written as a software component. Hence, it can be integrated in any other Python application. This was demonstrated by integrating Vision (Fig. 7A,B,F) with the freely available Python Molecular Visualization environment (PMV; Fig. 7D) developed at the MGL *(59)*. Exposing PMV objects such as molecules and PMV commands in Vision as node icons enabled the visual programming paradigm on these objects. For instance, Vision networks can call PMV commands, operate on molecules loaded in PMV, or modify the graphical representations of these molecules.

Combining Vision and PMV enabled designing, for example, novel techniques for the analysis and visualization of large supramolecular assemblies. The software was employed to build a novel 3D consensus model of the nuclear pore complex (NPC, see above; Fig. 3B). Heterogeneous data from cryo-EM, cryo-ET, and time-lapse SFM *(41)* was integrated in 3D using Vision's capabilities to load and isocontour volumetric as well as topographic data, which was added to the PMV 3D viewer. PMV's capabilities were employed to interactively place the various geometric parts in the resulting model (Fig. 3B). Furthermore, the tools allowed for advanced visualizations of the bluetongue virus [Fig. 7 *(55)*]. This viral capsid contains 900 proteins comprising almost 3 million atoms. By exploiting the icosahedral symmetry of the viral capsid, molecular data for only 15 proteins and less than 50,000 atoms need to be stored in memory, thus allowing real-time visualization of the complete capsid in various representations (Fig. 7D,E,G), furthering a more mechanistic understanding of viral capsid assembly.

Outlook

Nanobiotechnology mandates a highly multidisciplinary approach in education and research, cutting across the boundaries of biology, chemistry, physics, medicine, computer sciences, materials, and all aspects of engineering. Increasingly, the focus of research in nanobiotechnology and related fields is on obtaining reliable structural information of biological matter in different functional states and at different scales toward a mechanistic understanding of biological function. Scientists are now in the process of visualizing the machinery of life functions, atom-by-atom. The challenges they encounter lie not only in the enormous complexity of biological systems, but also in our ability to interact with, comprehend, and communicate the beauty and intricacy of this nano-world. New computational approaches such as discussed here are now needed to process, analyze, visualize, and validate the large and quickly growing data sets. These interdisciplinary efforts will pave the way towards discovery environments enabling us, for example, to visualize entire cells in atomic detail, and further our understanding of all processes of life.

Acknowledgments

This work was supported by the M.E. Müller Foundation of Switzerland, the Swiss National Science Foundation, and the Canto Basel Stadt. More specifically, the urothelial plaque project was supported by NIH grants DK52206, DK57269, and DK39753 (to X.P.K and T.T.S.) and by the National Centers of Competence in Research (NCCR) program on "Nanoscale Science" awarded by the Swiss National Science Foundation (to U.A.) and by the M.E. Müller Foundation of Switzerland. The nuclear pore complex project was supported by a Human Frontier in Science Program (HFSP) grant (to U. A.), an NCCR program grant on "Nanoscale Science" awarded by the Swiss National Science Foundation (to U.A.), the M.E. Müller Foundation of Switzerland, and a grant from the Chemical Industry Foundation of Basel (to D.S.). The articular cartilage project was supported by an NCCR program grant on "Nanoscale Science" awarded by the Swiss National Science Foundation (to U.A.), the M.E. Müller Foundation of Switzerland, and the Canton Basel-Stadt. Last, but not least, software development at The Scripps Research Institute (TSRI) was supported by a Swiss National Science Foundation grant (823A–61225) to D.S. and grants from the National Science Foundation and the National Institutes of Health to M.S. (NSF-NPACI, CA ACI9619020 and NIH NBCR, RR08605). This is TSRI manuscript number 17077-MB.

Fig. 7. (*Continued*) (**D**) Having individual geometry objects for each protein enables altering the visual representation of all symmetry-related copies of a particular protein (visible or not, solid rendering or lines, color, transparency, etc.). Here, chains A and B forming the inner shell are colored blue and cyan, respectively, and the container object "*inner Shell*" was modified from lines rendering to Gouraud shaded rendering. The 60 transformation matrices where only applied to chains A and B, while a single copy of the surfaces of the 13 proteins in the outer shell is shown. (**E**) (4x4)-Transformation matrices extracted using a "*Split*" node (see **F**) can be applied to any geometry. Here, five matrices corresponding to a pentamer are used to duplicate a ribbon diagram of the secondary structure, another five matrices are used to duplicate a carbon-alpha trace, and matrices corresponding to the upper-half of the capsid where applied to the outer shell container, while 45 matrices (i.e., 60 – 3*5 for the three pentamers missing) are applied to the inner shell container. (**F**) A "*Split*" node can be used to extract subsets of transformation matrices. Here, the five first matrices, which correspond to a pentamer in the capsid, are extracted and output on the second port of the "*Split*" node, while the remaining 55 matrices are output on the first port. (**G**) The bluetongue viral capsid half-shell depicting the inner- and outer shells.

References

1. Goodsell, D. S. (2004), *Bionanotechnology: lessons from nature*. Wiley-Liss, New York.
2. Steinmetz, M., Stoffler, D., Hoenger, A., Bremer, A., and Aebi, U. (1997), *J. Struct. Biol*. **119,** 295–320.
3. Orlova, E. V. and Saibil, H. R. (2004), *Curr. Opin. Struct. Biol*. **14,** 584–590.
4. Dubochet, J., Adrian, M., Chang, J. J., et al. (1988), *Q. Rev. Biophys.* **21,** 129–228.
5. Harrison, S. C. (2004), *Nat. Struct. Mol. Biol*. **11,** 293–295.
6. Fu, R. and Cross, T. A. (1999), *Annu. Rev. Biophys. Biomol. Struct.* **28,** 235–268.
7. Binning, G. and Rohrer, H. (1982), *Helv. Phys. Acta* **55,** 726.
8. Binning, G., Quate, C. F., and Gerber, C. (1986), *Phys. Rev. Lett*. **56,** 930–933.
9. Müller, D. J., Schabert, F. A., Büldt, G., and Engel, A. (1995), *Biophys. J.* **68,** 1681–1686.
10. Stoffler, D., Goldie, K. N., Feja, B., and Aebi, U. (1999), *J. Mol. Biol*. **287,** 741–752.
11. Stolz, M., Stoffler, D., Aebi, U., and Goldsbury, C. (2000), *J. Struct. Biol*. **131,** 171–180.
12. Tao, Y., Olson, N. H., Xu, W., Anderson, D. L., Rossmann, M. G., and Baker, T. S. (1998), *Cell* **95,** 431–437.
13. Raman, S., Machaidze, G., Lustig, A., Cole, J., and Burkhard, P. (2004), *Nat. Mat*, submitted.
14. Burkhard, P., Meier, M., and Lustig, A. (2000), *Protein Sci*, **9,** 2294–2301.
15. Burkhard, P., Ivaninskii, S., and Lustig, A. (2002), *J. Mol. Biol.* **318,** 901–910.
16. Burkhard, P., Stetefeld, J., and Strelkov, S.V. (2001), *Trends Cell Biol.* **11,** 82–88.
17. Tao, Y., Strelkov, S. V., Mesyanzhinov, V. V., and Rossmann, M. G. (1997), *Structure* **5,** 789–798.
18. Stetefeld, J., Frank, S., Jenny, M., et al. (2003), *Structure (Camb.)* **11,** 339–346.
19. Malashkevich, V. N., Kammerer, R. A., Efimov, V. P., Schulthess, T., and Engel, J. (1996), *Science* **274,** 761–765.
20. De Jong, M., Valkema, R., Jamar, F., et al. (2002), *Sem. Nucl. Med.* **32,** 133–140.
21. Aebi, U., Ten Heggeler, B., Onorato, L., Kistler, J., and Showe, M. K. (1977), *Proc. Natl. Acad. Sci. USA* **74,** 5514–5518.
22. Kistler, J., Aebi, U., Onorato, L., Ten Heggeler, B., and Showe, M. K. (1978), *J. Mol. Biol.* **126,** 571–589.
23. Buhle, E. L. and Aebi, U. (1984), *J. Ultrastruct. Res.* **89,** 165–178.
24. Bachmann, M. F. and Zinkernagel, R. M. (1996), *Immunol. Today* **17,** 553–558.
25. Nieba, L. and Bachmann, M. F. (2000), *Mod. Asp. Immunobiol.* **1,** 56–39.
26. Baschong, W., Hasler, L., Haner, M., Kistler, J., and Aebi, U. (2003), *J. Struct. Biol.* **143,** 258–262.
27. Zinkernagel, R. M. (1996), *Science* **271,** 173–178.
28. Hicks, R. M. (1975), *Biol. Rev. Camb. Philos. Soc.* **50,** 215–246.
29. Sun, T.-T., Liang, F. X., and Wu, X. R. (1999), *Adv. Exp. Med. Biol.* **462,** 7–18.
30. Hooton, T. M. and Stamm, W. E. (1997), *Infect. Dis. Clin. North Am.* **11,** 551–581.
31. Walz, T., Haner, M., Wu, X. R., et al. (1995), *J. Mol. Biol.* **248,** 887–900.
32. Min, G., Zhou, G., Schapira, M., Sun, T. T., and Kong, X. P. (2003), *J. Cell Sci.* **116,** 4087–4094.
33. Kachar, B., Liang, F., Lins, U., et al. (1999), *J. Mol. Biol.* **285,** 595–608.
34. Min, G., Stolz, M., Zhou, G., et al. (2002), *J. Mol. Biol.* **317,** 697–706.
35. Reichelt, R., Holzenburg, A., Buhle, Jr., E. L., Jarnik, M., Engel, A., and Aebi, U. (1990), *J. Cell Biol.* **110,** 883–894.
36. Fahrenkrog, B. and Aebi, U. (2003), *Nat. Rev. Mol. Cell Biol.* **4,** 757–766.
37. Jarnik, M. and Aebi, U. (1991), *J. Struct. Biol.* **107,** 291–308.
38. Panté, N. and Aebi, U. (1996), *Crit. Rev. Biochem. Mol. Biol.* **31,** 153–199.
39. Lutzmann, M., Kunze, R., Buerer, A., Aebi, U., and Hurt, E. (2002). Modular self-assembly of a Y-shaped multiprotein complex made from seven nucleoporins. *EMBO J*. **21,** 387–397.
40. Fahrenkrog, B., Koser, J., and Aebi, U. (2004), The nuclear pore complex: a jack of all trades? *Trends Biochem. Sci.*, **29,** 175–182.
41. Stoffler, D., Feja, B., Fahrenkrog, B., et al. (2003), *J. Mol. Biol*. **328,** 119–130.
42. Beck, M., Forster, F., Ecke, M., et al. (2004), *Science* **306,** 1387–1390.
43. Fahrenkrog, B., Maco, B., Fager, A., et al. (1992), *J. Struct. Biol.* **140,** 254–267.
44. Shah, S., Tugendreich, S., and Forbes, D. (1998), *J. Cell Biol.* 1998, **141,** 31–49.
45. Bastos, R., Lin, A., Enarson, M., and Burke, B. (1996), *J. Cell Biol.* **134,** 1141–1156.
46. Pasterkamp, G., Falk, E., Woutman, H., and Borst, C. (2000), *J. Am. Coll. Cardiol*. **36,** 13–21.
47. Sinclair, D. A., Smith, I. R., Wickramasinghe, H. K., and McAvoy, B. R. (1982), *Ultrasonics Symposium Proceedings IEEE*, New York, NY, Vol 2, p. 1090.
48. Stolz, M., Raiteri, R., Daniels, A. U., VanLandingham, M. R., Baschong, W., and Aebi, U. (2004), *Biophys. J.* **86,** 3269–3283.
49. Hunziker, P., Stolz, M., and Aebi, U. (2002), *Chimia* **56,** 520–526.
50. Oberleithner, H., Schneider, S. W., Albermann, L., et al. (2003), *J. Membr. Biol*. **196,** 163–172.
51. Rotsch, C. and Radmacher, M. (2000), *Biophys. J.* **78,** 520–535.
52. Stolz, M., Imer, R., Staufer, U., and Aebi, U. (2003), *Bioworld* 2–4, www.bioworld.ch.
53. Stolz, M., Imer, R., Staufer, U., Friederich, N. F., and Aebi, U. (2004), http://www.nccr-nano.org/nccr/media/nanonews/nanonews_03.
54. Sanner, M. F. (2005), Using the Python Programming Language for Bioinformatics. *Encyclopedia of Genomics, proteomics and bioinformatics*. Addision-Wesley, John Wiley & Sons, Ltd. (in press).
55. Sanner, M. F. (2005), *Structures,* Special issue in visualization, simulation and representation of biological complexes (in press).
56. Lutz, M. (2001), Programming Python 2nd ed. O'Reilly & Associates, Inc., Sebastapol,CA, www.python.org.
57. Sanner, M. F. (1999), *J. Mol. Graphics Mod*. **17,** 57–61.
58. Sanner, M. F., Stoffler, D., and Olson A. J. (2002), In: *Proceedings of the 10th International Python Conference.* February 4–7, 2002, pp.103–115.
59. Stoffler, D., Coon, S. I., Huey, R., Olson, A. J., and Sanner, M. F. (2003), In: *Proceedings of the Thirty-Sixth Annual Hawaii International Conference on System Sciences (CD/ROM),* January 6–9, 2003, Computer Society Press.